Optical Modeling with 2-D Fresnel Analysis for Micromachined Acoustic Transducers

Sundeep Jolly

1 Introduction

Recent advances in optical interferometric sensing schemes for acoustic transduction applications have led to the advent of micromachined acoustic sensors with higher scalability than those employing capacitive sensing schemes [1]. A recent diffraction-based interferometric displacement sensing scheme has been proposed [1] and implemented [1], [2] in a micromachined optical microphone.

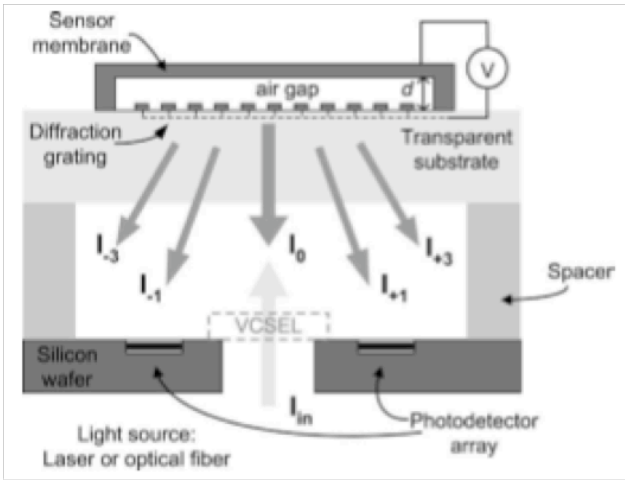

Figure 1: [Adapted from [3]]. Cross-section of the optical microphone showing the placement of the VCSEL and sensing electronics with the orientation of the grating and membrane.

As shown in Fig. 1, the acoustic transduction scheme consists of a sensor membrane (i.e., diaphragm) with an integrated diffraction grating. A pulsed vertical cavity surface emitting laser (i.e., VCSEL) is employed as a low-power light source for the sensing scheme. Interferometric sensing of the displacement of the sensor membrane is accomplished through post-processing of the intensities of the diffracted orders as retrieved by a fixed photodiode array. A simple scalar-based analysis of the reflected field in the ideal case (i.e., grating much larger than beam spot size, low beam divergence) shows that the intensities of the diffracted orders arriving at the photodiode plane (i.e., I_0 and $I_{\pm 1}$) are a function of the gap thickness and can be expressed as:

$$I_0 = I_{in} \cos^2\left(\frac{2\pi d_0}{\lambda_0}\right) \tag{1}$$

and

$$I_{\pm 1} = \frac{4I_{in}}{\pi^2} \sin^2\left(\frac{2\pi d_0}{\lambda_0}\right) \tag{2}$$

where λ is the VCSEL operating wavelength and I_{in} is the incident VCSEL beam intensity. There is a clear modulation effect as the arriving intensities for the 0th and $\pm$1st diffracted orders are a function of the gap thickness and are out-of-phase with respect to one another.

This simple analysis does not account for the non-uniform spatial intensity of the VCSEL beam or the finite size of the grating. Additionally, assumptions of far-field (i.e., Fraunhofer) diffraction are employed when the actual compact dimensions require near-field (i.e., Fresnel) analysis. Therefore, a more detailed approach to modeling is required.

Previous approaches to more detailed models for the interferometric displacement sensor have relied on diffraction analysis using the Huygens integral along with ray-transfer matrix analysis [3]. However, this model employs the paraxial approximation and is therefore unable to account for generalized tilted or curved surfaces or off-axis elements. A model utilizing a full two-dimensional Fresnel analysis has been developed to investigate the effect of the offset grating and tilted membrane that are present in the actual structure on the retrieved diffraction efficiency and modulation efficiency and is described here.

2 Methods for Optical Analysis

A previous approach to modeling the overall interferometric displacement sensing scheme is detailed by

Hall *et al.* [3]. As mentioned earlier, this model employs two simplifying assumptions which limit the validity and accuracy of the results. First, the grating is modeled as being infinite when in reality the overall grating dimensions may be smaller than the beam spot size at the grating plane. Second, the reflective sensing membrane is assumed to be flat (i.e., the arriving beam is normally incident) when in reality the membrane has some slight tilt. Additionally, the finite grating may be offset from the VCSEL optical axis. Because of these limitations, the earlier ray-transfer matrix analysis cannot be used. The model presented

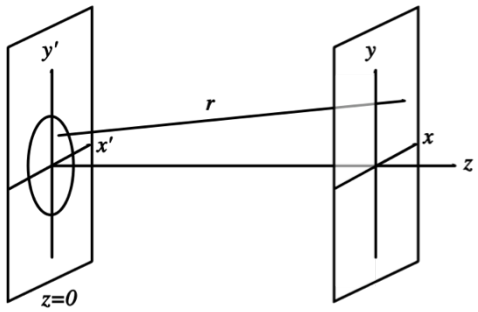

Figure 2: [Image is in the public domain]. Scheme of diffraction geometry for Fresnel (near-field) diffraction. The aperture (input) plane is given on the left and the image (output) plane is given on the right.

here employs a full 2-D analysis using the Fresnel (i.e., near-field) approximation to the well-known Huygens diffraction integral to relate the optical fields at input (i.e., object) planes to those at output (i.e., image) planes some distance z away. The generalized diffraction geometry for this type of analysis is shown in Fig. 2. The resulting output field $U_o(x, y)$ is related to the input field $U_i(x, y)$ by:

$$U_o\left(x, y, z\right) = \frac{e^{jkz}}{j\lambda z} e^{\frac{jk}{2z}\left(x^2+y^2\right)} \cdot H\left(\nu_x = \frac{x}{\lambda z}, \nu_y = \frac{y}{\lambda z}\right) \tag{3}$$

where

$$H\left(\nu_x, \nu_y\right) = F\left\{U_i\left(x',\ y'\right) \cdot e^{\frac{jk}{2z}\left(x'^2+y'^2\right)}\right\} \tag{4}$$

In the above expressions, $k = 2\pi/\lambda$ is the wavevector and F represents the 2-D Fourier transform.

The VCSEL output at the VCSEL plane can be modeled as a Gaussian field distribution as:

$$U_1\left(x, y\right) = \sqrt{\frac{2P_0}{\pi w_0^2}} \ \cdot \ e^{-\left(\frac{x^2+y^2}{w_0^2}\right)} \tag{5}$$

where P_0 is the VCSEL output power and w_0 is the beam waist (which is related to the beam divergence angle by $\theta_{div} = \lambda/\pi \cdot w_0$).

The field U_2 arriving at the grating plane is calculated using Eqs. 3 and 4 with the input field U_1 as defined in Eq. 5. At the grating plane, only a fraction of the arriving field U_2 is incident on the finite grating. To model this, the field U_2 is multiplied by a windowing function in two-dimensions corresponding to the finite dimensions g_x and g_y of the grating. If the grating is offset in the y-direction, then the windowing function is set to be offset by y_0. The overall windowed field is then given by:

$$U_2'\left(x, y\right) = \Pi\left(\frac{x}{g_x}\right) \Pi\left(\frac{y\ +\ y_0}{g_y}\right) U_2\left(x, y\right) \tag{6}$$

The portion of the windowed field that passes through the grating slits is reflected by the sensor membrane. Since the gap thickness d between the grating plane and the sensor membrane is small, the ray theory is employed and the portion of the field passing through the grating slits acquires a relative phase shift of $\phi = 4d\pi/\lambda$ with respect to the field directly reflecting from the grating fingers and the region outside the finite grating. If the membrane displacement is not uniform (e.g., in the case of a tilted membrane), this is accounted for by a spatial variation of d as $d(x, y)$. If the membrane is tilted in the y-direction by a tilt

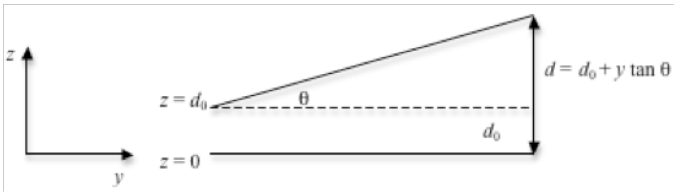

Figure 3: Geometry for the tilted membrane in y-direction with tilt angle θ_{tilt}.

angle θ_{tilt} (see Fig. 3), then the thickness function d is expressed as $d(y) = d_0 + y \cdot tan\theta_{tilt}$, where d_0 is the initial gap thickness between the grating plane and the lowest point on the tilted membrane.

The overall reflected field from the grating plane is a result of the reflection of the portion of the field U_2 passing through the grating slits from the sensor membrane and also the reflection of remaining portion of the field from the polysilicon grating fingers and region outside the finite grating. If the power reflection coefficient of the sensor membrane is 1 and the power reflection coefficient of the polysilicon layer

is R, then the overall reflected field from the grating plane is (after simplifying algebra):

$$U_{2R}(x,y) = A(x,y) \cdot U_2(x,y) \tag{7}$$

where

$$A(x,y) = \left[\Pi\left(\frac{x}{g_x}\right)\Pi\left(\frac{y+y_0}{g_y}\right)G(x)\left(e^{j\phi(y)} - R\right) + R\right] \tag{8}$$

and

$$G(x) = \sum_{n=-\infty}^{\infty} \Pi\left(\frac{x - n\Lambda}{\frac{\Lambda}{2}}\right) \tag{9}$$

is the grating function modeled as a square wave with grating period Λ and 50% duty cycle. The field U_3 arriving at the photodiode plane is calculated using Eqs. 3 and 4 with the input field U_{2R} as defined in Eq. 7.

In order to calculate the power retrieved by the photodiodes from the arriving field U_3, the modulus-squared of the field is integrated over the photodiode active area and then multiplied by a proportionality constant as:

$$P = \frac{c\epsilon_0}{2}\int\int_A |U_3(x,y)|^2\, dxdy \tag{10}$$

where A is region on the photodiode plane representing the photodiode active area, c is the speed of light in vacuum, and ϵ_0 is the permittivity of free space. For the purposes of this model, the photodiode positions for capturing the 0th and $\pm$1st orders can be set at any position on the photodiode plane in order to maximize the retrieved power. In this paper, the modulation effect of varying the gap thickness between grating and sensing membrane on the arriving power at the photodiode array will be shown using optical curves. Modulation efficiency is used as a measure of the performance of the overall interferometric displaement sensor and is defined here as $\eta_{mod} = (max(P) - min(P))/max(P)$ where P is the optical curve being considered.

3 Model Implementation and Results

MATLAB is used to implement the described model. Relevant parameters for the modeling are listed in Table 1.

To illustrate the functionality of the model in predicting the behavior of the interferometric displacement sensor, an ideal case with a well-collimated VCSEL beam (i.e., low divergence angle of $\theta_{div} = 1.5°$) is considered first. In an ideal situation, we consider the well-collimated beam with an infinite grating so that none of the power is lost due to truncation by a finite grating. Example arriving field profiles at the photodiode plane due to the interference of the reflection from the grating fingers and that from the sensor membrane are shown in Fig. 4 for acquired round-trip phase shifts of the field passing through the grating slits of $\phi = 0$, $\phi = \pi/2$, and $\phi = \pi$.

Table 1: Operating parameters for the optical modeling.

VCSEL Operating Wavelength λ	850 nm
VCSEL Nominal Output Power P_0	2.0 mW
Distance from VCSEL to grating plane z	900 μm
Distance from grating to photodiodes L	850 μm
Finite grating x-dimension g_y	100 μm
Finite grating y-dimension g_y	100 μm
Grating offset in y-direction y_0	-50 μm
Photodiode active area diameter	100 μm

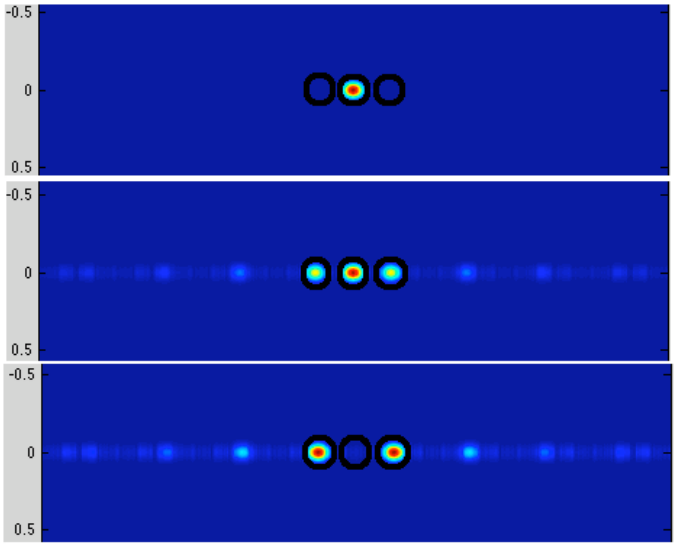

Figure 4: Profile of field arriving at photodiode plane with $\theta_{div} = 1.5°$ and an infinite grating. In this case, the reflectivity of the grating fingers is 1. Acquired phase shift in gap between grating plane and membrane, top to bottom: $\phi = 0$, $\phi = \pi/2$, and $\phi = \pi$. Photodiode positions and active area regions used for detection of the diffracted orders are indicated.

Note that in the $\phi = 0$ case, the grating-membrane system acts as a perfect reflector. The profiles show that the arriving power is a maximum for the 0th or-

der (and minimum for the ±1st orders) for $\phi = 0$ and is a maximum for the ±1st orders (and minimum for the 0th order) for $\phi = \pi$. Also note that because of the small beam divergence, there is no apparent overlap in the x-direction of the diffracted orders. The optical curves showing the modulating effect of varying the gap thickness on the arriving power at the photodiode array are shown in Fig. 5.

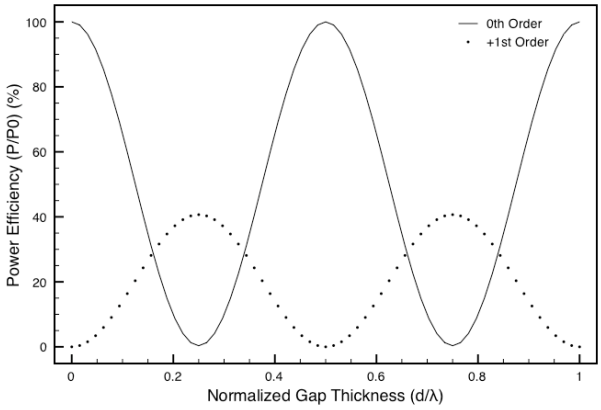

Figure 5: Effect of modulating gap thickness d on retrieved optical power for the 0th and +1st order photodiodes for the ideal case being considered here with $\theta_{div} = 1.5°$. The power arriving at the photodiodes is normalized to the VCSEL output power P_0.

In the case shown, the photodiodes have a circular active area with diameter 175 μm and are centered at the theoretical order locations (i.e., (x,y) = (0 μm, 0 μm) for the 0th order and (x,y) = (192.5 μm, 0 μm) for the 1st order. These parameters allow for capturing of over 99% of the power diffracted into each order. Note that the powers arriving for the 0th and 1st orders are 180° out of phase. Also note that this result is consistent with the earlier result from the simple scalar diffraction theory and interference analysis in Eqs. 1 and 2.

This ideal case shows the functionality of the model in predicting the modulation effect of varying the gap thickness on the diffracted order intensities. However, a more realistic model will take into account real characteristics of the implemented acoustic transducer (e.g., finite grating, off-axis grating, tilt of sensor membrane, and large VCSEL beam divergence). To begin illustrating how these characteristics affect the performance of the interferometric sensing scheme, the well-collimated example (i.e., $\theta_{div} = 1.5°$) will be extended to cases with a finite grating and tilted sensor membrane.

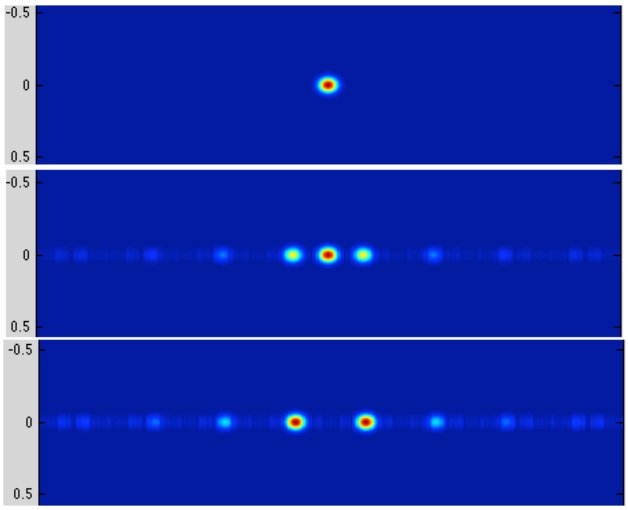

Figure 6: Profile of field arriving at photodiode plane with $\theta_{div} = 1.5°$ and a finite grating with grating dimensions (g_x, g_y) = (100 μm, 100 μm). In this case, the reflectivity of the grating fingers is 1 and the reflectivity of the region outside the finite grating is 0. Acquired phase shift in gap between grating plane and membrane, top to bottom: $\phi = 0$, $\phi = \pi/2$, and $\phi = \pi$.

The resulting field profiles arriving at the photodiode plane with an on-axis (i.e., not offset) finite grating with dimensions (g_x, g_y) = (100 μm, 100 μm) are shown in Fig. 6 for relative phase shifts of $\phi = 0$, $\phi = \pi/2$, and $\phi = \pi$. Note that even with the finite grating, the field profiles appear the same as for an infinite grating (as seen in Fig. 4) due to the small VCSEL beam divergence (i.e., the finite grating does not truncate the field at the grating plane sufficiently to significantly alter its diffraction and reflection behavior).

To illustrate the effect of tilting the sensor membrane, the case with an on-axis finite grating is considered for a membrane that is tilted in the y-direction. Sample resulting field profiles for this case are shown in Fig. 7 for tilt angles $\theta_{tilt} = 0.2°$, $\theta_{tilt} = 0.5°$, and $\theta_{tilt} = 1.0°$.

Note that the resulting field profiles are due to the phasor-sum of the field arriving from the reflection from the tilted membrane and that arriving due to the reflection from the grating fingers. With increasing tilt angle, interference fringes in the y-direction become evident due to the interference of the field arriving from the polysilicon layer reflection and that

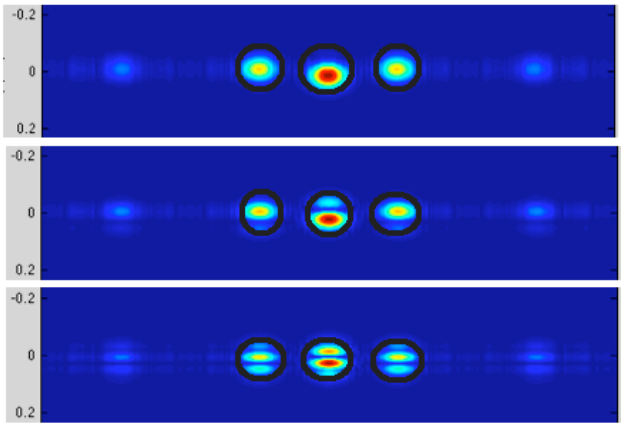

Figure 7: Effect of membrane tilt angle on profiles of fields arriving at photodiode plane with $\theta_{div} = 1.5°$ and a finite grating with grating dimensions (g_x, g_y) = (100 μm, 100 μm). In all cases, the average acquired phase shift over y in the region of the finite grating is $\phi = \pi/2$ (i.e., point of maximal sensitivity in modulation). Membrane tilt angle, top to bottom: $\theta_{tilt} = 0.2°$, $\theta_{tilt} = 0.5°$, and $\theta_{tilt} = 1.0°$. In this case, the reflectivity of the grating fingers is 1 and the reflectivity of the region outside the finite grating is 0. The photodiode positions and active area regions for detecting the diffracted orders are indicated as shown.

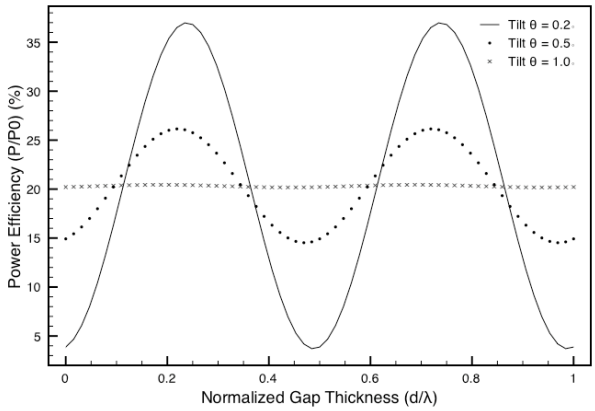

Figure 8: Optical curve generated for the tilted cases with $\theta_{tilt} = 0.2°$, $\theta_{tilt} = 0.5°$, and $\theta_{tilt} = 1.0°$. Note that the power efficiency shown is that captured for the +1st order photodiode.

from the tilted membrane. The optical curves showing the modulation effect of varying the initial gap thickness d_0 are shown in Fig. 8 (note here that the same configuration for the photodiodes as before is used again).

This result clearly shows that although the modulation effect remains as the tilt angle θ_{tilt} increases, the modulation efficiency η_{mod} drops. This relationship is examined more fully in Fig. 9.

Note that the retrieved modulation efficiency is highly sensitive to the tilt angle, as even a tilt angle of 0.8° results in modulation efficiency close to 0%. This type of behavior is expected as the interference between fields becomes increasingly less pronounced as the tilt angle increases (see, e.g., Fig. 7). A similar analysis of the average power efficiency η_{pow} as a function of the tilt angle θ_{tilt} is shown in Fig. 10.

Because the field arriving from the tilted membrane increasingly does not overlap with the photodiode active area as the tilt angle increases, the retrieved power drops with increasing tilt angle. Note that this drop in average arriving power efficiency is not as pro-

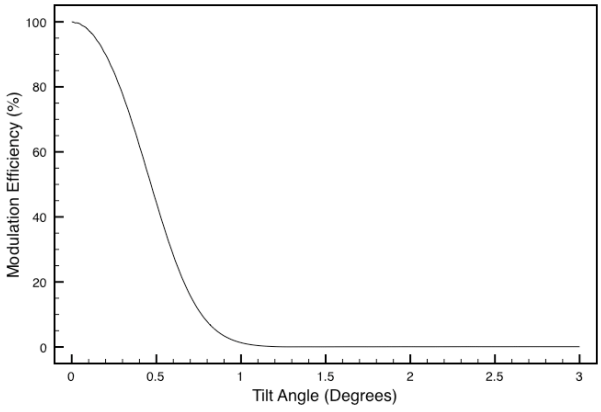

Figure 9: Relationship between membrane tilt angle and retrieved modulation efficiency for the +1st order photodiode.

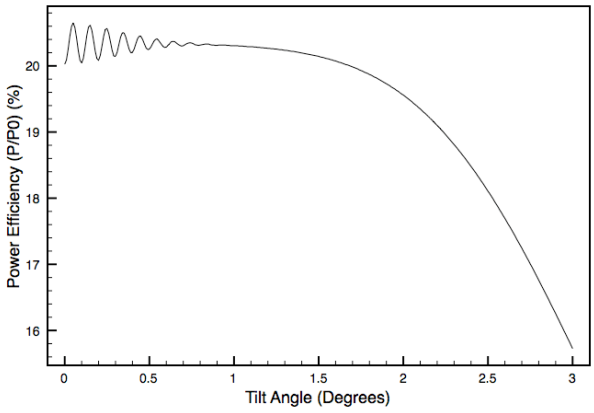

Figure 10: Relationship between membrane tilt angle and retrieved average power efficiency (i.e., $P_{+1,captured}/P_0$) for the +1st order photodiode.

nounced for small tilt angles as compared to the drop in modulation efficiency for small tilt angles. Also note that the retrieved average power efficiency falls to some DC level (due to the constant reflection from the grating fingers) as the tilt angle increases and the field arriving from the reflection from the tilted membrane is displaced off the photodiode active area.

After considering the effects of the structural non-idealities (e.g., off-axis grating and membrane tilt) with an ideal (i.e., well-collimated) VCSEL beam on the arriving field profiles and performance of the displacement sensor, it is important to consider the effect of a more realistic VCSEL beam output characteristic. The VCSEL type used in the implemented transducer packages has a divergence angle nearly equal to $\theta_{div} = 8^\circ$ and this case is considered at this point. The arriving field profiles for the high-divergence case with an infinite grating and flat sensor membrane are shown in Fig. 11 for relative phase shifts $\phi = 0$, $\phi = \pi/2$, and $\phi = \pi$.

With the high beam divergence, note that one begins to see an overlap of the diffracted orders in the x-direction. This acts to decrease the retrieved modulation efficiency because of the interference of the orders. The optical curve demonstrating the modulation effect when varying the gap thickness is shown in Fig. 12. In the case considered here, the photodiodes have a circular active area with diameter 175 μm and are centered at (x,y) = (0 μm, 0 μm) for the 0th order and (x,y) = ($\pm$192.5 μm, 0 μm) for the $\pm$1st order (i.e., same configuration as used before in small

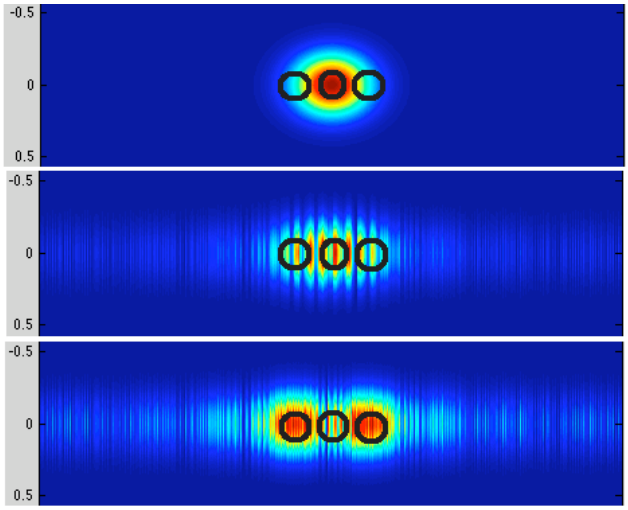

Figure 11: Profile of field arriving at photodiode plane with $\theta_{div} = 8^\circ$ and an infinite grating. In this case, the reflectivity of the grating fingers is 1 and the reflectivity of the region outside the finite grating is 0. Acquired phase shift in gap between grating plane and membrane, top to bottom: $\phi = 0$, $\phi = \pi/2$, and $\phi = \pi$. Note the overlap of the diffracted orders in the x-direction with the large divergence angle. Photodiode positions and active area regions for detecting the diffracted orders are indicated.

divergence angle case).

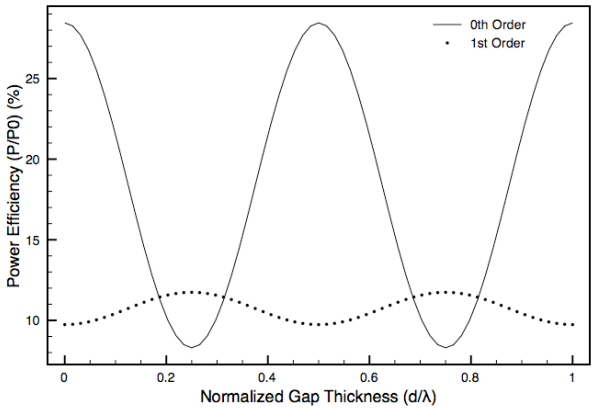

Figure 12: Effect of modulating gap thickness d on retrieved optical power for the 0th and +1st order photodiodes for the ideal case being considered here with $\theta_{div} = 8°$. The power arriving at the photodiodes is normalized to the VCSEL output power P_0.

Note that the arriving power efficiency for the large divergence case is a fraction of that for the small divergence case, mainly because of the small area of the photodiode active area with respect to the area of the arriving orders on the photodiode plane. Also, note that the modulation efficiency drops from 100% in the small divergence case (for both the 0th and 1st order photodiodes) to 70.8% for the 0th order photodiode and 17.1% for the 1st order photodiode in the large divergence case, mainly because of the interference of overlapping diffracted orders.

The arriving field profiles for the large beam divergence case with a finite grating are shown in Figs. 13.

A brief examination of the result of setting the reflectivity of the region outside the finite grating to something other than $R = 0$ is shown in Fig. 14. Note that the reflectivity for the region outside the grating and the reflectivity for the grating fingers are set the same value ($R = 0.2$) since these are presumed to be the same polysilicon material in the implementation (with the grating created by simply etching away the slit regions).

Note the shape of the arriving field profiles reflects the truncation of the field due to the finite grating since the divergence angle is large. Also note the "halo" effect around the center region due to the reflection from the region outside the finite grating. It is noted that this more realistic case leads to an increased modula-

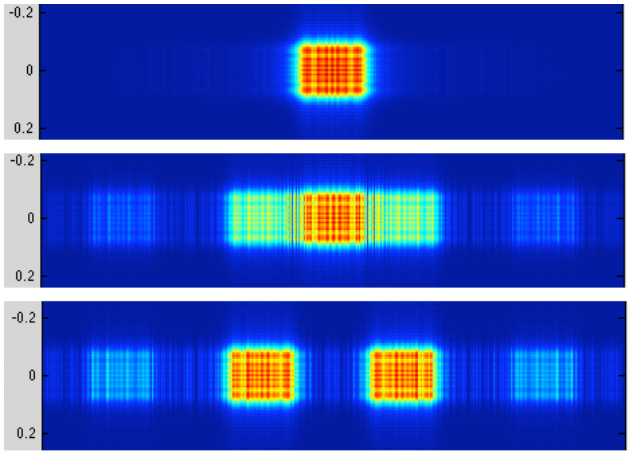

Figure 13: Profile of field arriving at photodiode plane with $\theta_{div} = 8°$ and a finite grating with grating dimensions $(g_x, g_y) = (100\ \mu\text{m}, 100\ \mu\text{m})$. In this case, the reflectivity of the grating fingers is 1 and the reflectivity of the region outside the finite grating is 0. Acquired phase shift in gap between grating plane and membrane, top to bottom: $\phi = 0$, $\phi = \pi/2$, and $\phi = \pi$.

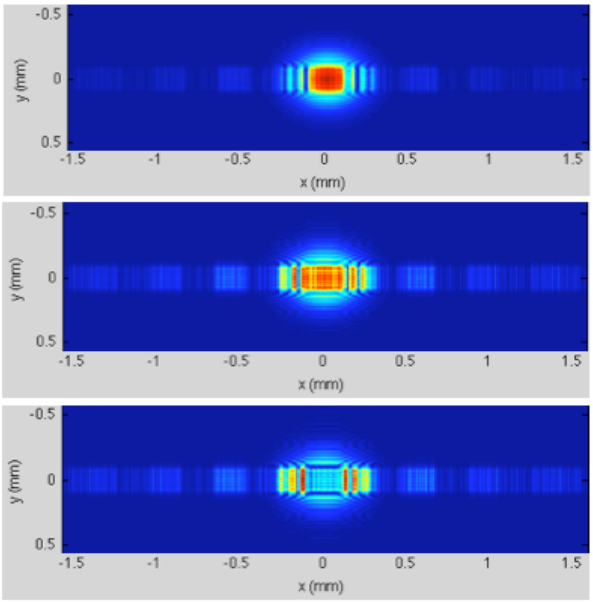

Figure 14: Profile of field arriving at photodiode plane with $\theta_{div} = 8°$ and a finite grating with grating dimensions $(g_x, g_y) = (100\ \mu\text{m}, 100\ \mu\text{m})$. In this case, the power reflection coefficient for the grating fingers and the region outside the finite grating is $R = 0.2$ (a typical value for polysilicon). Acquired phase shift in gap between grating plane and membrane, top to bottom: $\phi = 0$, $\phi = \pi/2$, and $\phi = \pi$.

tion efficiency because the effect of the intereference of the fields arriving from the reflection from the sensor membrane and from the reflection from the polysilicon layer is more pronounced.

While the implemented model has the capability to retrieve the field profiles arriving at the photodiode plane for cases with a large VCSEL divergence angle, membrane tilt, and offset grating, further cases are not considered here.

4 Conclusions and Future Work

The model is able to predict the modulative behavior of the displacing the sensor membrane on the arriving power well. Non-idealities in the structure of the interferometric displacement sensing scheme (e.g., off-axis finite grating, membrane tilt) can be accounted for. Additionally, the model is robust and able to handle a variety of parameter sweeps and input conditions.

There are, however, limitations of the model that need to be considered when assessing the overall validity. In its current state, the model neglects multiple reflections and transmissions in the region between the grating plane (polysilicon layer) and reflective membrane. The transmissive properties of the polysilicon layer are neglected but need to be considered for a more complete analysis of the behavior. Also, the model is reverting to ray theory when considering what happens to the field that passes through the grating slits and reflects from the sensor membrane. This approach may not describe the complete optical behavior when considering large divergence angles.

The modeling shows that the largest detriment to the performance of the overall optical readout scheme is the beam divergence of the VCSEL. Additional detriments to the overall retrieved modulation efficiency and power efficiency include the offset of the grating with respect to the center of the VCSEL beam, tilt of the reflective membrane, and parasitic diffractive effects due to the finite grating. Also, performance of the overall system in terms of modulation efficiency and power efficiency can be improved by optimization of the placement of the photodiodes at the photodiode plane and the distance between the grating plane and the photodiode plane.

Several potential approaches to decrease the divergence of the VCSEL beam and improve the intensity profile arriving at the photodiode array are being considered. For our structure, it is ideal to have either a collimating optical element integrated with the VCSEL or a planar element for collimation and perhaps steering of the beam in the spacing between the VCSEL and grating plane.

Diffractive micro-Fresnel lenses have been demonstrated to collimate the output of laser diodes where the divergence angle is over 10° [4], [5]. Furthermore, the Fresnel microlenses can be made to be planar and allow for simple integration with VCSELS [6], [7]. Additionally, Fresnel lenses can be used for beam collimation, bending using off-centered elements in addition to the focusing application.

Generalized diffractive optical elements (e.g., Fresnel zone plates) have been shown to have certain advantages in resolution over classical planar Fresnel lenses for applications in collimation and beam-guiding [8]. Additionally, their integration into MOEMS systems is generally simpler than that of classical Fresnel lenses since all they require is etching of the requisite surface-relief profiles [8].

References

[1] W. Lee, N. Hall, Z. Zhou, and F. Degertekin, "Fabrication and Characterization of a Micromachined Acoustic Sensor With Integrated Optical Readout," *IEEE Journal of Selected Topics in Quantum Electronics* vol. 10, no. 3, 643-651 (2004).

[2] N. Hall, M. Okandan, R. Littrell, B. Bicen, and F. Degertekin, "Micromachined optical microphone structures with low thermal-mechanical noise levels," *Journal of the Acoustic Society of America* vol. 122, no. 4 (2007).

[3] N.A. Hall, W. Lee and F. L. Degertekin, "Capacitive Micromachined Ultrasonic Transducers with Diffractionbased Integrated Optical Displacement Detection," *IEEE Transactions on Ultrasonics, Ferroelectrics, and Frequency Control* vol. 50, pp. 1570-1580 (2003).

[4] Ogata, S.; Sekii, H.; Maeda, T.; Goto, H.; Yamashita, T.; Imanaka, K., "Microcollimated laser diode with low wavefront aberration," *IEEE Photonics Technology Letters*, vol.1, no.11, pp.354-355, Nov 1989

[5] Blum, O.; Kilcoyne, S.P.; Warren, M.E.; Du, T.C.; Lear, K.L.; Schneider, R.P., Jr.; Carson, R.F.; Robinson, G.; Peters, F.H., "Vertical-cavity surface-emitting lasers with integrated re-

fractive microlenses," *Electronics Letters*, vol. 31, no. 1, Jan. 1995.

[6] K. Rastani, M. Orenstein, E. Kapon, and A. C. Von Lehmen, "Integration of planar Fresnel microlenses with vertical-cavity surface-emitting laser arrays," *Optics Letters* 16, 919-921 (1991)

[7] Kasra Rastani, Abdellatif Marrakchi, Sarry F. Habiby, William M. Hubbard, Harold Gilchrist, and Robert E. Nahory, "Binary phase Fresnel lenses for generation of two-dimensional beam arrays," *Applied Optics* 30, 1347-1354 (1991)

[8] M. Rossi, R. E. Kunz, and H. P. Herzig, "Refractive and diffractive properties of planar micro-optical elements," *Applied Optics* 34, 5996-6007 (1995).